Magnetic Multimaterial Printing for Multimodal Shape Transformation with Tunable Properties and Shiftable Mechanical Behaviors

Chunping Ma,[†] Shuai Wu,[†] Qiji Ze, Xiao Kuang, Rundong Zhang, H. Jerry Qi, and Ruike Zhao*

Cite This: *ACS Appl. Mater. Interfaces* 2021, 13, 12639−12648

Read Online

ACCESS | Metrics & More | Article Recommendations | SI Supporting Information

ABSTRACT: Magnetic soft materials (MSMs) have shown potential in soft robotics, actuators, metamaterials, and biomedical devices because they are capable of untethered, fast, and reversible shape reconfigurations as well as controllable dynamic motions under applied magnetic fields. Recently, magnetic shape memory polymers (M-SMPs) that incorporate hard magnetic particles in shape memory polymers demonstrated superior shape manipulation performance by realizing reprogrammable, untethered, fast, and reversible shape transformation and shape locking in one material system. In this work, we develop a multimaterial printing technology for the complex structural integration of MSMs and M-SMPs to explore their enhanced multimodal shape transformation and tunable properties. By cooperative thermal and magnetic actuation, we demonstrate multiple deformation modes with distinct shape configurations, which further enable active metamaterials with tunable physical properties such as sign-change Poisson's ratio. Because of the multiphysics response of the M-MSP/MSM metamaterials, one distinct feature is their capability of shifting between various global mechanical behaviors such as expansion, contraction, shear, and bending. We anticipate that the multimaterial printing technique opens new avenues for the fabrication of multifunctional magnetic materials.

KEYWORDS: programmable soft materials, magnetic actuation, shape memory polymers, multimaterial 3D printing, direct ink writing, active metamaterials
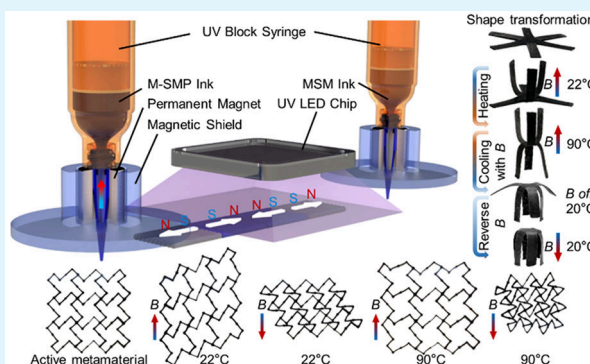
INTRODUCTION

Programmable shape-changing soft materials that respond to stimuli including heat,[1−3] light,[4−6] and electric[7,8] or magnetic fields[9,10] have drawn special interest in the developments of soft robotics,[11−13] actuators,[14−16] metamaterials,[17,18] and biomedical devices.[19−21] Among a variety of emerging stimuli-responsive soft materials, magnetic soft materials (MSMs) composed of magnetic particles embedded in soft polymeric matrices show great application potential because they are capable of untethered, fast, and reversible shape reconfigurations as well as controllable dynamic motions under applied magnetic fields.[9,11,22−24] When actuated by an external magnetic field, the magnetic particles can generate microtorques to deform the matrix to align the composite's magnetization to the direction of the external field, leading to complex shape transformations. The recent advances in 3D printing of MSMs further promote the programmability of the predesigned magnetization distribution in the material, realizing functional shape configurations under magnetic fields.[25] To enhance the functionalities of magnetic-responsive soft composites, researchers have recently developed magnetic shape memory polymers (M-SMPs) by embedding hard magnetic particles in thermoresponsive shape memory polymers to enable untethered, fast, and reversible actuation and shape locking.[26] A thermoresponsive M-SMP can transfer from a stiff "glassy state" to a soft "rubbery state" by heating it above its glass-transition temperature (T_g). Its rubbery behavior allows fast and reversible actuation with large deformation under the external magnetic field, showing similar behaviors as MSMs. When the temperature is lower than T_g, the M-SMPs show glassy behavior with a stiffness that is orders of magnitude higher than the stiffness at the rubbery state, preventing any forms of large deformation and shape change. Therefore, any deformed shapes of M-SMPs above T_g can be locked by maintaining the external magnetic field while cooling the temperature to below T_g. The operation of the M-SMP utilizes temperature and magnetic fields to cooperatively control the shape morphing for more deformation modes,
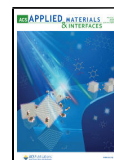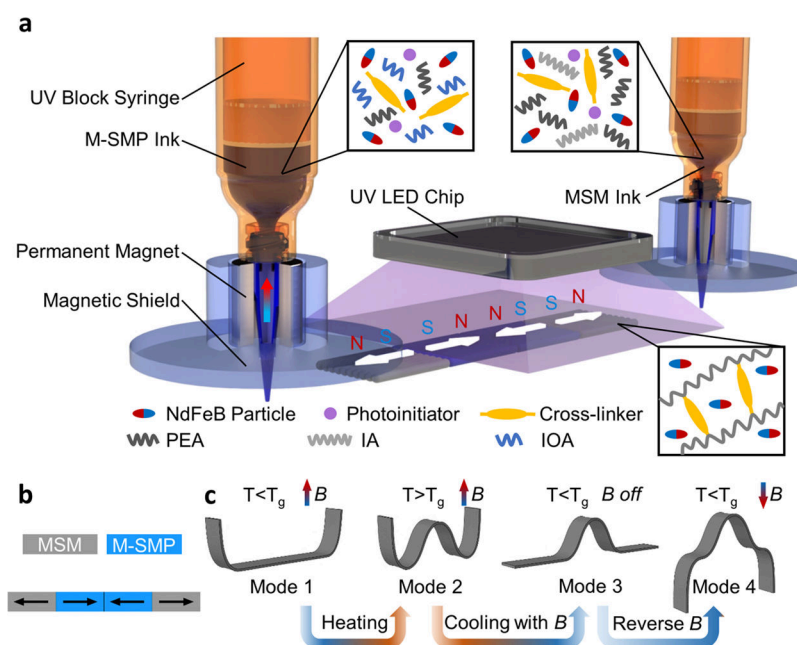
Figure 1. Magnetic multimaterial DIW(M^{3}DIW) system and working mechanism. (a) Schematic of the M^{3}DIW fabrication and material composition. (b) Material distribution and magnetization directions of a one-dimensional M-SMP/MSM stripe with four segments. (c) Four different deformation modes achieved by cooperatively controlling the temperature and magnetic field.

providing more flexibility for applications that require integrated shape manipulations.

Recently, material systems that are composed of multiple materials with distinct properties, or so-called multimaterials, have demonstrated success in expanding the design domain of advanced materials for integrated functionalities. For example, controllable physical properties and behaviors such as tunable material stiffness,[16,27] strength,[28] negative thermal expansion,[29−31] negative swelling,[17,32] and negative Poisson's ratio[33] are accomplished by various multimaterial systems via the integration of materials with different physical properties. The functionality of the aforementioned multimaterials relies on not only the carefully designed material systems but also the fabrication methods to effectively implement the complex material integration, which has been greatly promoted by the recent development of 3D printing techniques such as stereolithography,[1,34,35] fused deposition modeling,[36−38] direct ink writing (DIW),[39−42] and integrated technique.[43]

In this work, we present a magnetic multimaterial DIW (M^{3}DIW) technique for the complex structural integration of photocurable M-SMP and MSM to explore their enhanced multimodal shape transformation with tunable properties and shiftable mechanical behaviors. Figure 1a schematically shows the M^{3}DIW fabrication system and the main composition of the inks. Two types of magnetic composite inks, M-SMP and MSM, composed of uncured photocurable polymeric resins, photoinitiators, magnetized neodymium−iron-boron (NdFeB) microparticles, and fumed silica nanoparticles as a rheological modifier, are loaded in the ultraviolet (UV) block syringes. The photocurable resins are prepared by two different recipes of monomers and cross-linker (see Materials and Methods for more details) for synthesizing materials with distinct temperature-dependent material properties. The monomers include 2-phenoxyethanol acrylate (PEA), isobornyl acrylate (IOA), and isodecyl acrylate (IA), and the cross-linker is aliphatic urethane diacrylate (AUD). After being loaded into the syringes, the M-SMP and MSM inks embedded with NdFeB particles are

magnetized under a 1.5 T impulsive magnetic field. During the printing, the programmed magnetization is achieved by reorienting the particles' polarities to the longitudinal direction of the nozzles, where a printing magnetic field around 180 mT is induced by a ring-shaped magnet. To protect the magnetization of the already-printed structure from the influence of the printing magnetic field, we added a steel magnetic shield at the nozzle tip to mitigate the intensity of the magnetic field. By controlling the switching between the two syringes as well as the printing directions, MSM and MSMP can be structurally integrated into the design. The direction of the printing magnetic field and the magnetization of the printed structure are shown in Figure 1a. An LED chip emitting 385 nm wavelength UV light is utilized to cure the resins after printing. After curing, MSM is soft at room temperature, whereas M-SMP has a T_g around 60−70 °C.

The multimodal shape configuration of the M-SMP/MSM composites relies on the cooperative stimulation by both the magnetic field and temperature change. Here, we use a simple one-dimensional M-SMP/MSM stripe to illustrate the operation mechanism. The magnetization distribution and the four deformation modes are depicted in Figure 1b,c, respectively. At room temperature (lower than the T_g of M-SMP), only the MSM parts can deform when applying an actuation magnetic field, whereas the M-SMP parts stay undeformed because of the high stiffness, forming the deformation Mode 1 with a "U" shape. Upon the removal of the magnetic field, the deformed shape returns to the undeformed configuration, demonstrating fast-transforming capability. When the operating temperature is above T_g, both materials can be actuated by the magnetic field, forming the Mode 2 with a "W" shape. Next, by maintaining the magnetic field and cooling the structure to below T_g, the M-SMP parts lock into the deformed shape, whereas the MSM parts return to their undeformed configuration once the magnetic field is removed, leading to the shape in the Mode 3 with a peak at the center. Finally, applying a reversed magnetic field to the
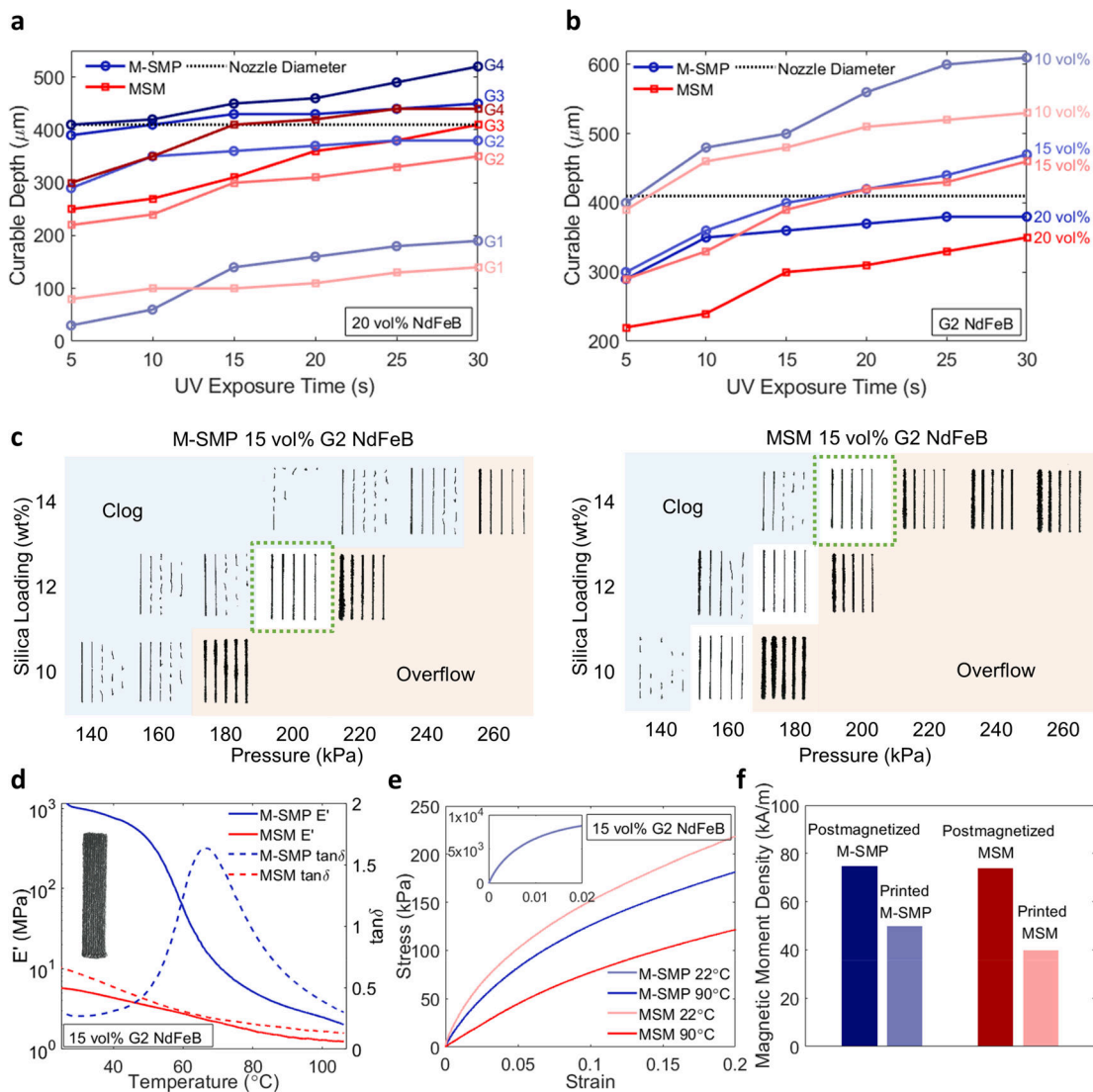
Figure 2. Characterizations of the inks and the printed materials. (a) Effects of NdFeB particle size and UV exposure time on the curable depth of the inks with 20 vol % NdFeB particle loading. (b) Effects of NdFeB loading and UV exposure time on the curable depth of the inks with G2 (37 ± 6 μm) particles. (c) Effects of silica loading, printing pressure, and nozzle translation speed on the quality of the printed filament. Each grid shows five filaments printed at different nozzle translation speeds, which increase from 5 to 25 mm/s with a step of 5 mm/s from left to right. (d) Storage modulus E' and tan δ versus temperature of M-SMP and MSM using 15 vol % G2 NdFeB. The T_g of M-SMP is measured as 66 °C. The printed specimen (20 mm × 4 mm × 0.4 mm) for the characterization is shown on the left. (e) Tensile tests of M-SMP and MSM using 15 vol % G2 NdFeB at 22 and 90 °C. (f) Magnetic moment densities of M-SMP and MSM using 15 vol % G2 NdFeB particles.

structure in the Mode 3 results in the wavy deformation in the Mode 4. Note that another set of four vertically symmetric deformation modes can be easily obtained by reversing all the directions of the external magnetic field in Figure 1c. By conducting finite-element (FE) simulations,[44] the responses of the magnetic multimaterial structures can be precisely predicted, guiding the designs for desired multimodal actuation.

RESULTS AND DISCUSSION

Ink Characterization. The success of multimaterial DIW printing of the M-SMP/MSM composites depends on the printability of the ink and its curing efficiency and quality. In M³DIW, the inks are extruded from nozzles with predetermined diameters and then cured by UV light, where two major ink properties influence the printing and curing process, i.e., the rheological property and the curable depth of the ink. The

former property can be tuned by adjusting the loading of fumed silica nanoparticles that serve as a rheological modifier. The latter property is mainly determined by the particle size and loading of the NdFeB microparticles as well as the UV exposure time and intensity.

The curable depth of different inks under a preset UV light is studied first to select the proper NdFeB particle size for printing. To investigate the effect of NdFeB particle size and loading on the curing depth, we prepare four groups of particles with different sizes (G1, 22.5 ± 7.5 μm; G2, 37 ± 6 μm; G3, 58 ± 16 μm; G4, 112 ± 38 μm). We test M-SMP and MSM inks made from each group of NdFeB at a fixed loading of 20 vol %. Here, 10 wt % silica nanoparticles with respect to the neat resin are added to maintain the inks in a paste state. Note that the introduction of silica particles mainly tunes the rheological property of the ink without changing the curable depth. Figure 2a shows the measured curable depth of each ink
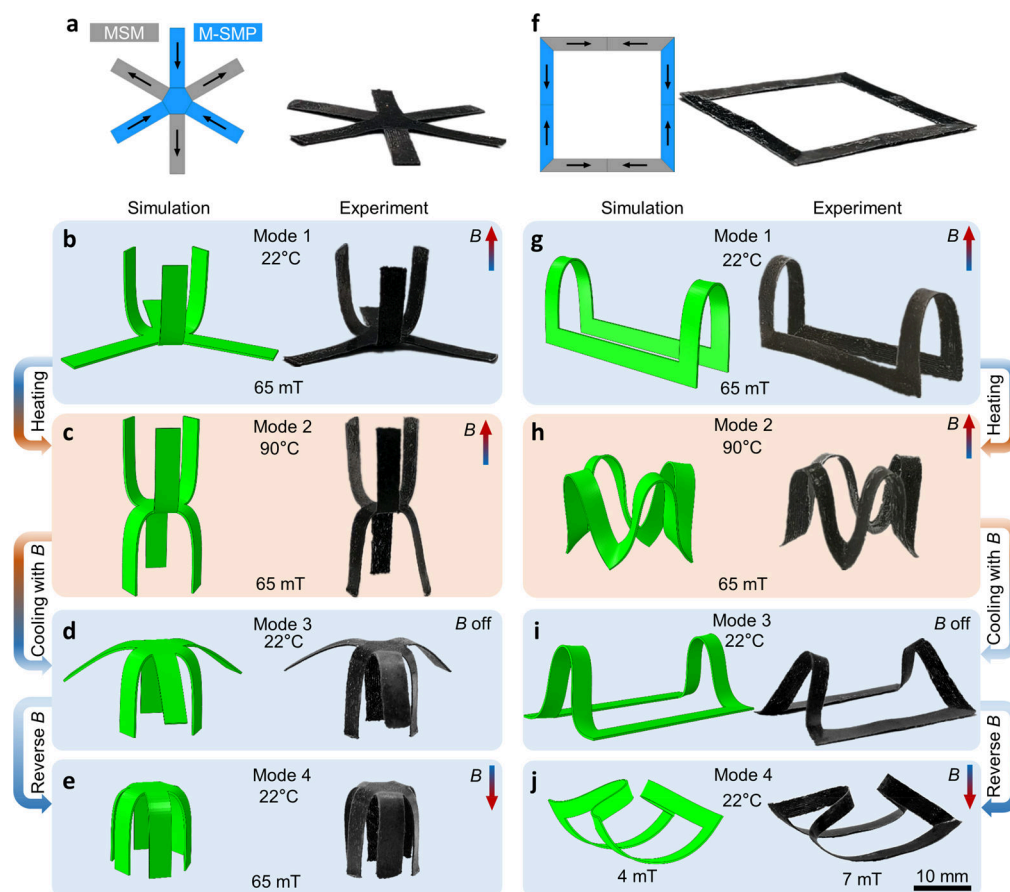
Figure 3. Schematic designs, simulations, and experiments of M-SMP/MSM composites for multimodal pop-up actuation. (a–e) Asterisk design with alternating material distribution and magnetization directions. (f–j) Square frame design with inward-pointing magnetization directions.

with different exposure times from 5 to 30 s, showing that the curable depths of all inks increase with the particle size and the exposure time, and most of the inks converge to certain curable depths with 30 s UV exposure. To successfully cure a printed layer, the curable depth of the ink should reach at least the diameter of the printing nozzle (410 μm, black dashed line in Figure 2a) within a certain exposure time. Although larger NdFeB particle size shows better curing performance, it in the meantime increases the risk of clogging the nozzle during printing due to the formation of large clusters of the magnetized particles under the printing magnetic field. Therefore, G2 particles (37 $\pm$ 6 μm) are selected for the printing ink, as it is small enough to prevent clogging during printing while maintaining a good curable depth. Figure 2b illustrates the effect of different particle loadings of G2 to the curable depth with respect to UV exposure time, indicating that for both M-SMP and MSM, using 15 vol % G2 NdFeB can achieve a curable depth larger than the nozzle diameter with a UV exposure time longer than 20 s. Based on the investigation of NdFeB particles' effect on curing, we finally choose 15 vol % G2 particles for both M-SMP and MSM inks with a 30 s exposure time as the printing parameters to satisfy the requirement of the curable depth and printing quality.

Reliable rheological properties and proper printing pressures of M-SMP and MSM inks are crucial to enable the successful printing of multilayer 3D structures. To tune the ink viscosity for the optimized printability and quality, fumed silica nanoparticles are added as a rheological modifier for both inks, as increasing the silica particle loading can effectively

increase the viscosity of the ink. In addition, a higher printing pressure can lower the viscosity due to the shear-thinning behavior of the inks. To investigate the optimized silica particle loading, we prepared M-SMP and MSM inks with fixed 15 vol % G2 NdFeB particles (with respect to the ink) and 10, 12, and 14 wt % silica loadings (with respect to the neat resin) for printing under different printing pressures. As shown in Figure 2c, 30 mm long filaments of M-SMP and MSM are printed by varying the nozzle translation speed from 5 to 25 mm/s with a step of 5 mm/s and the printing pressure from 140 to 260 kPa with a step of 20 kPa. The distance between the nozzle tip and the printing substrate is fixed to 0.4 mm. The printing qualities of different inks at varied conditions are summarized in two phase diagrams in Figure 2c. Each grid contains five filaments printed at five different nozzle translation speeds increasing from left to right. Enlarged pictures of the printed filaments are shown in Figure S2. The printing test shows that the ink must reach a certain viscosity to retain its printed shape and prevent overflowing. However, if the ink viscosity is too high, it tends to clog the nozzle unless the printing pressure is further increased. For the M-SMP, 12 wt % silica with 200 kPa pressure (highlighted by the green dash line) is the optimal combination that shows no obvious accumulation nor discontinuity of the ink for all the tested nozzle translation speeds. For MSM, though the combinations of 10 wt % and 160 kPa, 12 wt % and 180 kPa, and 14 wt % and 200 kPa seem to yield similar filament shapes, we sometimes observe phase separation of uncured resin and magnetic particles after printing the MSM inks using 10 and 12 wt % silica for a
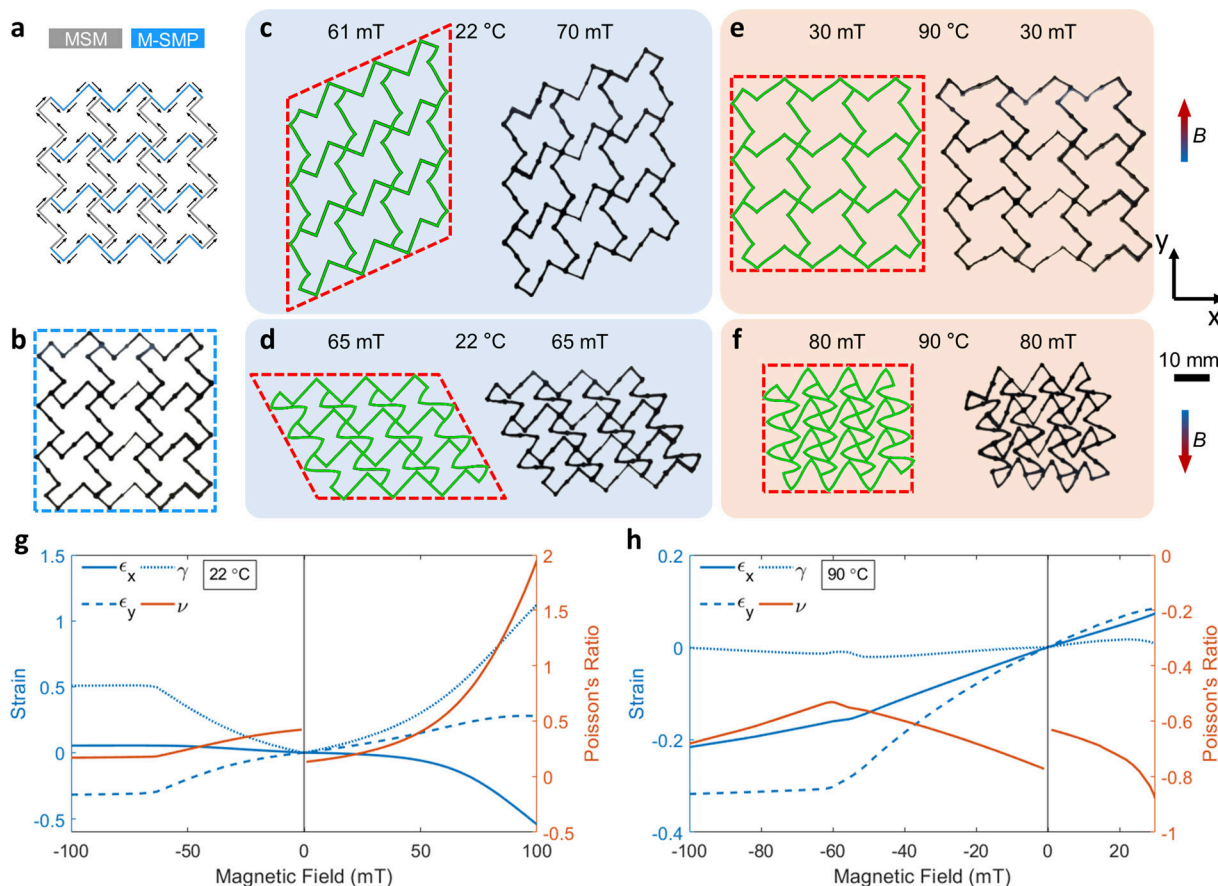
Figure 4. M-SMP/MSM metamaterial with tunable Poisson's ratio and shear deformation using a chiral design. (a) Schematic of the material and magnetization distributions. (b) Printed metamaterial. (c, d) Simulations and experiments of the deformed shapes at 22 °C under (c) upward and (d) downward magnetic fields. (e, f) Simulations and experiments of the deformed shapes at 90 °C under (e) upward and (f) downward magnetic fields. (g, h) Strains and Poisson's ratio versus magnetic field (upward as positive, downward as negative) at (g) 22 and (h) 90 °C obtained from simulations.

longer time. Thus, an MSM ink with 14 wt % silica is used for the following printing. Though a higher speed is advantageous for faster fabrication process, we choose 10 mm/s to ensure filament continuity. With the well-tuned rheological properties of the inks, a certain number of printed filaments can be directly stacked up and stand on their own without extra supporting structures, enabling the fast 3D printing of multilayered structures.

Figure 2d depicts the thermomechanical properties of M-SMP and MSM. The picture of a printed thin-film specimen (20 mm × 4 mm × 0.4 mm) for the test is also shown. With the temperature increasing from 22 °C (room temperature) to 105 °C, the storage modulus E' of the M-SMP drops significantly from 1.16 GPa to 2.02 MPa, whereas the modulus of MSM goes through a relatively slight change from 5.75 to 1.24 MPa. The T_g of M-SMP is measured as 66 °C, where tan δ reaches its maximum value. Figure 2e shows the nominal stress versus nominal strain from the tensile tests of printed M-SMP and MSM specimens at 22 and 90 °C, which are set to be the operating temperatures for following demonstrations of the M-SMP/MSM composites. It can be further seen that M-MSP is at its glassy state at 22 °C and it shows rubbery behavior at 90 °C. On the contrary, MSM shows rubbery behavior at both 22 and 90 °C. The Young's moduli of M-SMP at 22 and 90 °C are measured as 1.16 GPa and 2.04 MPa, respectively, and those of MSM are 1.64 and 0.89 MPa, respectively (see

Mechanical and Magnetic Characterization of Materials for details).

Figure 2f shows the remanence of M-SMP and MSM specimens, characterized by the magnetic moment density. The printed M-SMP and MSM specimens with the printing magnetic field yield 50 and 40 kA m^{-1}, respectively. To evaluate the reorientation effectiveness of the printing magnetic field on the premagnetized ink, we also measured the specimens that are postmagnetized after printing as the reference. The measured results of M-SMP and MSM are 75 and 74 kA m^{-1}, respectively. The printing magnetic field can achieve 67% and 54% of the magnetic moment densities of the postmagnetized M-SMP and MSM samples, respectively. The lower magnetic moment density of the printed MSM could be due to the higher viscosity brought by the higher silica loading of MSM. The measured Young's moduli of the material at 22 and 90 °C and the magnetic moment densities of the printed M-SMP and MSM then serve as the input parameters for FE simulations to predict the shape configurations under thermal and magnetic stimulations.

Pop-up Structures with Multimodal Actuation. Showing the capability of reliable printing of M-SMP/MSM composites via M³DIW, here we present two pop-up structures to demonstrate how the multimodal shape transformation is implemented through the cooperative control of the magnetic field and temperature. For an M-SMP/MSM composite, the
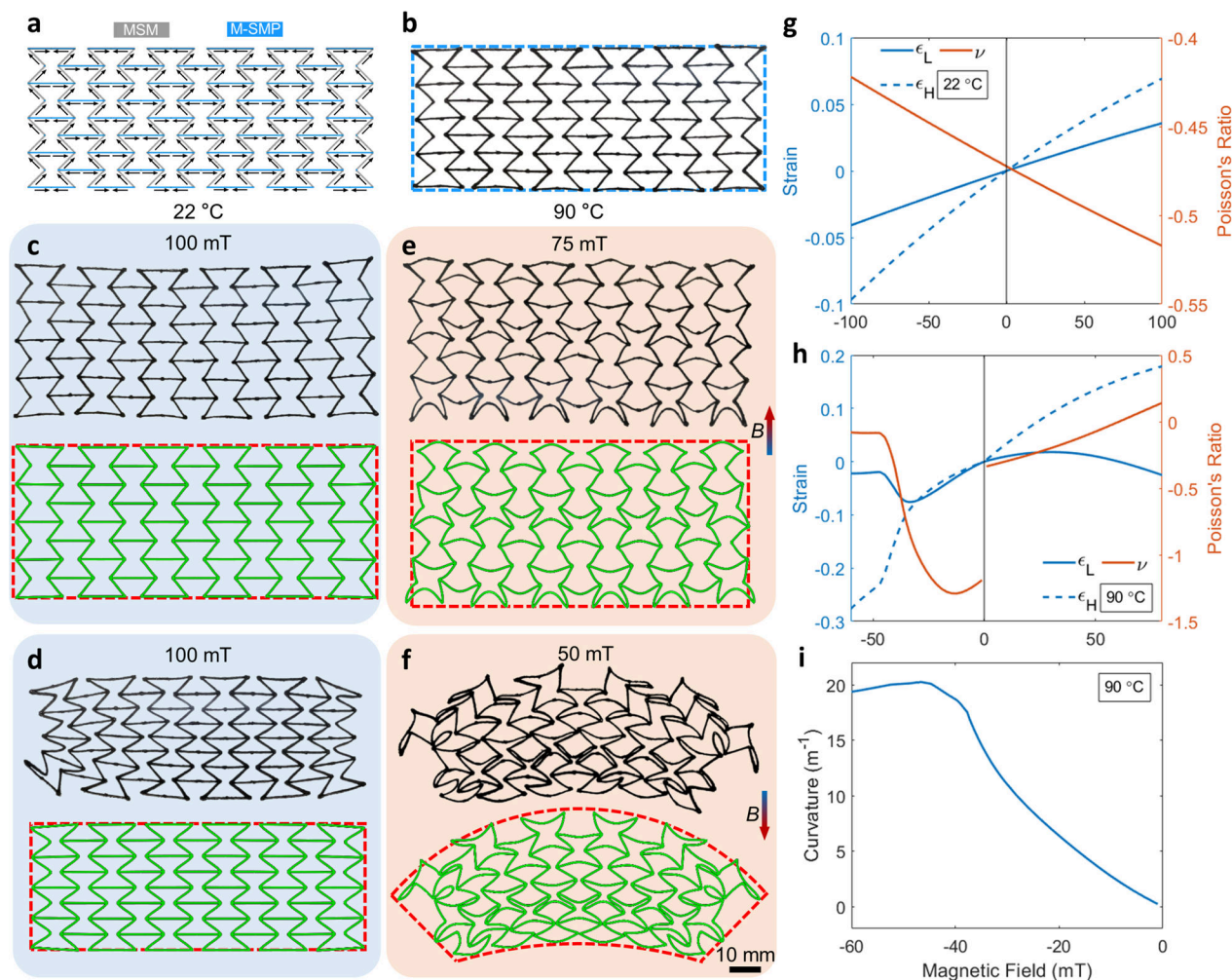
Figure 5. M-SMP/MSM metamaterial with tunable Poisson's ratio and bending deformation using an hourglass design. (a) Schematic of the material and magnetization distributions. (b) Printed metamaterial. (c, d) Simulations and experiments of the deformed shapes at 22 °C under (c) upward and (d) downward magnetic fields. (e, f) Simulations and experiments of the deformed shapes at 90 °C under (e) upward and (f) downward magnetic fields. (g, h) Strains and Poisson's ratio versus magnetic field (upward as positive, downward as negative) at 22 °C (g) and 90 °C (h) obtained from simulations. (i) Curvature versus magnetic field of the bending deformation under a downward magnetic field at 90 °C obtained from simulation.

MSM parts provide fast and reversible magnetic actuation at both 22 and 90 °C, while the M-SMP parts can only be actuated when the operating temperature is above T_g (90 °C in the demonstrations). By controlling the thermal and magnetic loading path, multiple deformation modes can be achieved. In Figure 3a, the left part shows the material and magnetization distributions of an asterisk design with six arms, a printed sample of which is shown on the right. Figure 3b−e show four deformation modes of the asterisk design from both simulations and experiments (see Video S1). The blue and orange backgrounds indicate the operating temperature at 22 and 90 °C, respectively. It can be seen that our FE simulations show good agreements with the experiments, and thus can be used to guide the design process. Upon the application of an upward magnetic field (65 mT), three MSM arms of the initial 2D shape bend up to form the deformation Mode 1 at 22 °C (Figure 3b). By increasing the operating temperature to 90 °C, while keeping the magnetic field, the three M-SMP arms bend down to form the Mode 2 (Figure 3c) with a doubled aspect ratio compared to the Mode 1. Next, by cooling the composite under the applied magnetic field, the M-SMP arms lock their

deformed shapes, and the Mode 3 with flattened MSM arms can be achieved by removing the magnetic field at this point as the MSM is incapable of shape locking without magnetic actuation (Figure 3d). Finally, a reversed (downward) magnetic field bends MSM arms to the same direction of the M-SMP ones with slightly different deflection to form the Mode 4 (Figure 3e). Note that the multiple deformation modes not only demonstrate various shape configurations, but also switch the symmetry of the design from the 6-fold symmetry of the undeformed configuration to the 3-fold symmetry of the four deformed configurations.

Next, we present a square frame design with an initial 4-fold symmetry, with material and magnetization distribution shown in Figure 3f. The four deformation modes following the same path of thermal and magnetic loadings are illustrated in Figure 3g−j (also see Video S1). Under an upward magnetic field, the MSM stripes bend and change the structural symmetry from the undeformed 4-fold to deformed 2-fold (Mode 1, Figure 3g). When increasing the temperature from 22 to 90 °C, the new configuration Mode 2 switches back to 4-fold symmetry (Figure 3h) under the same applied magnetic field. After being

cooled down, it turns to 2-fold symmetry again in the Mode 3 (Figure 3i) and the Mode 4 (Figure 3j) with different deformations. For each of the aforementioned designs capable of multimodal shape transformation, we can obtain another set of four deformation modes by reversing the directions of all the external magnetic fields in Figure 3.

Active Metamaterials with Tunable Properties. Active metamaterials are architected material systems whose internal structure/tessellation can be changed under external stimulations.[2,17,18,32,45−47] The local shape configuration of the metamaterials has been demonstrated to provide global property tunability.[32,48−52] In this section, we exploit M-SMP/MSM composites for active metamaterial designs to show how the multimodal shape transformation promotes functional material systems with widely tunable physical properties, including sign change of Poisson's ratio, tunable shear, and bending deformation.

Figure 4a shows the schematic of the architecture and the magnetization of the M-SMP/MSM active metamaterial with a chiral design. The printed sample is shown in Figure 4b. Figure 4c−f illustrate the deformations obtained from simulations and experiments at different temperatures and magnetic fields, showing good agreement between the simulations and the experiments. The actuation processes are shown in Video S2. It can be seen that the actuation of the metamaterial is dominated by significant shear deformation at 22 °C (Figure 4c,d), under both the upward and downward magnetic fields. However, by actuating the metamaterial at 90 °C, the deformations indicate mainly biaxial expansion under the upward magnetic field (Figure 4e) or contraction under the downward magnetic field (Figure 4f) with negligible shear. Interestingly, the thermal and magnetic coupled loadings demonstrate a controllable shift between different mechanical behaviors, such as the shear and biaxial deformations in the presented chiral metamaterial. This is due to the selective actuation at 22 °C, where only the MSM parts can deform, leading to the actuated configuration that distorts and breaks the global structural symmetry. At 90 °C, both materials exhibit similar elastic stiffnesses and can deform simultaneously, and thus the whole composite retains its global structural symmetry while being actuated.

To quantitatively evaluate the deformation and mechanical property changes of the metamaterial, we measure the normal strain ε_x and ε_y, shear strain γ, and Poisson's ratio ν versus magnetic field (upward as positive, downward as negative) from the simulation results, as shown in Figure 4g,h. The calculations of the strains are illustrated in Figure S3. Because the magnetic field is applied in the y-axis, the Poisson's ratio is defined as $\nu = -\varepsilon_x /\varepsilon_y$. At 22 °C, the chiral metamaterial shows increased shear strain with the increasing magnetic field intensity in either upward or downward directions. The normal strains are relatively small and a positive Poisson's ratio is observed. It is noteworthy that under the negative magnetic field, all the strains reach a plateau at 63 mT because of the contact among the layers of unit cells. At 90 °C, the chiral metamaterial exhibits biaxial contraction under the downward magnetic field and biaxial expansion under the upward magnetic field with negative Poisson's ratios, and the shear strain is negligible. Therefore, by changing the operating temperature of the M-SMP/MSM chiral metamaterial, one can change the sign of the Poisson's ratio, in the meantime shift its mechanical behaviors between shear and biaxial deformations. Note that in Figure 4c, the magnetic field required in the

simulation differs from that in the experiment. Possible reasons related to the uncertain experimental factors include the friction between the metamaterial and the substrate, the uneven thickness of the printed filaments, and the structural discrepancy due to the ink accumulation at the filament joints.

Another M-SMP/MSM metamaterial using an hourglass design is shown in Figure 5. Figure 5a,b show the schematic and the printed sample, respectively. Figure 5c−f show the simulations and experiments of the metamaterial actuation at different operating temperatures and magnetic fields (also see Video S3). At 22 °C, the biaxial expansion and contraction are obtained under the upward (Figure 5c) and downward (Figure 5d) magnetic fields, respectively. The selective actuation opens or closes the lateral MSM edges of the unit cell while keeping the horizontal M-SMP edges undeformed. Note that there is a small deformation discrepancy between the experiments and simulation at the lateral edges of the metamaterial, which is due to the free boundary condition and the slightly inhomogeneous magnetic field spanning in the horizontal direction. At 90 °C, global expansion is observed under the upward magnetic field (Figure 5e). However, the deformation of the hourglass metamaterial shifts to a bending behavior when switching the magnetic field to the downward direction (Figure 5f). This bending deformation is a result of the coupling of the magnetization distribution and the free boundary condition at the metamaterial edges. Although the total torque induced by the magnetization distribution of the metamaterial cancels out under the applied magnetic field, the local torque generated on each beam leads to significant distortion of the unit cells especially for the ones at the edges. As these cells are freer to deform asymmetrically because of the less symmetric constraint compared with the unit cells in the middle, their deformations thus guide the global actuation shape of the metamaterial. This can be seen by looking at the unit cells at two lateral edges, where three of the five vertices on each side tend to bend downward, leading to the global downward bending of the whole metamaterial. Note that the beams connected by the same vertex tend to fold together under the downward magnetic field, forming an acute angle that is easier to bend. On the contrary, obtuse angles at the vertices are formed at the lateral edges under an upward magnetic field, making bending difficult. This is the reason that biaxial deformation is dominant in Figure 5e.

In Figure 5g−i, we quantitatively evaluate the deformation of the hourglass metamaterial by the normal strain ε_L and ε_H (the subscript "L" and "H" are for length and height, respectively), Poisson's ratio ν, and bending curvature versus magnetic field (upward as positive, downward as negative) from the simulation results. The Poisson's ratio is defined as $\nu = -\varepsilon_L/\varepsilon_H$. The definitions of the measurements are illustrated in Figure S4. Here, the global shear deformation is negligible and is not presented. At 22 °C, negative Poisson's ratio is obtained during either the contraction or expansion, as elucidated in Figure 5g. At 90 °C, the metamaterial shows a sign-switching Poisson's ratio under the increasing upward magnetic field and a negative Poisson's ratio under the downward magnetic field due to biaxial contraction as shown in Figure 5h. Figure 5i illustrates the bending curvature of the metamaterial under the downward magnetic field at 90 °C, where it first increases with the field intensity until 47 mT, and then reaches a plateau due to the contact among unit cells.

From the two M-SMP/MSM metamaterial designs, the multiple deformation modes provided by the thermomagnetic

coupled actuation demonstrate not only the tunable mechanical property as discussed by the deformation-sensitive Poisson's ratio, but also provide controllable shifting between various mechanical responses including expansion, contraction, shear, and bending. This capability of integrating multiple mechanical responses into one metamaterial system has not been seen in existing active metamaterials, where simple expansion and contraction are mostly seen.[17,29,53] With the wide structural tunability under the cooperative thermal and magnetic actuation, the proposed M-SMP/MSM metamaterials intrinsically accompany other tunable physical properties such as global stiffness, anisotropy, porosity, acoustic bandgap, and many others.

CONCLUSIONS

In this work, we present the magnetic multimaterial printing technology that enables the integrated 3D printing of the magnetic shape memory polymer and magnetic soft material. Through the cooperative thermal and magnetic actuation of the M-SMP/MSM composites, a series of pop-up designs with multimodal deformation are demonstrated. Two M-SMP/MSM metamaterials are designed to illustrate the tunable Poisson's ratio and metamaterial's capability of shifting between different mechanical behaviors such as shear, biaxial deformation, and bending under programmed thermal and magnetic actuation. Although this paper involves only two material inks, it is easy to incorporate more types of functional material inks into the current printing system for more integrated functionalities. We envision that the magnetic multimaterial printing technology will serve as a robust fabrication method for magnetic materials with integrated multiphysics and multifunctional responses for the future development of morphing structures, soft robotic systems, and biomedical devices.

MATERIALS AND METHODS

Ink Formulation and Preparation. In this paper, the initial liquid resins of M-SMP and MSM matrices are acrylate-based amorphous polymers with different compositions. The neat M-SMP resin is composed of aliphatic urethane diacrylate (Ebecryl 8413, Allnex, Alpharetta, GA, USA), 2-phenoxyethanol acrylate (Allnex, Alpharetta, GA, USA), and isobornyl acrylate (Sigma-Aldrich, St. Louis, MO, USA), with a weight ratio of 15:30:55. The neat MSM resin is composed of aliphatic urethane diacrylate, 2-phenoxyethanol acrylate, and isodecyl acrylate (Sigma-Aldrich, St. Louis, MO, USA), with a weight ratio of 10:80:10. Phenylbis (2,4,6-trimethylbenzoyl) phosphine oxide is used as the photoinitiator (1.5 wt % to the resin) to induce free radical polymerization for both M-SMP and MSM. The chemical structures of each component are shown in Figure S1. The fumed silica nanoparticles (12 wt % to the resin for M-SMP, and 14 wt % for MSM) with an average size of 0.2−0.3 μm (Sigma-Aldrich, St. Louis, MO, USA) are added as a rheological modifier to increase the ink viscosity and impart shearing thinning to achieve desired printability. The initial liquid resin is first mixed with the fumed silica nanoparticle by a planetary mixer (AR-100, Thinky, Laguna Hills, CA, USA) at 2,000 rpm for 4 min, following by manual mixing to further break the silica aggregates. After another 2 min of mixing at 2000 rpm, sieved NdFeB microparticles (average size of 25 μm, MQFP-B-2007609−089, Magnequench, Anderson, IN, USA) within the range of 37 ± 6 μm (G2) and the photoinitiator are added following by 4 min of mixing at 2000 rpm. Then the ink is transferred into a 10 cc UV-block syringe barrel (7012126, Nordson EFD, Providence, RI, USA) and defoamed in the mixer at 2200 rpm for 30 s to remove the trapped air. Finally, the ink is magnetized by a 1.5 T impulse magnetic field applied by an in-house built impulse magnetizer.

M³DIW Process. After installing the printing nozzles (7018298, SmoothFlow Tapered Tips, 410 μm inner diameter, Nordson EFD, Providence, RI, USA), the two syringe barrels loaded with magnetized M-SMP and MSM inks are mounted to a customized gantry 3D printer (Aerotech, Pittsburgh, PA, USA). A ring-shaped NdFeB permanent magnet with a steel magnetic shield is then attached to each nozzle. The air pressure to each syringe barrel is individually powered by a high-precision dispenser (7012590, Ultimus V, Nordson EFD, Providence, RI, USA). The initial pressure is set according to the experiment results in Figure 2c. Before printing, the relative position of the two syringe nozzles is calibrated to guarantee accuracy. The printing process is controlled by the printing G-code generated from CADFusion (Aerotech, Pittsburgh, PA, USA). After printing, the printed structure is exposed to a 100-W UV LED chip of 385 nm wavelength (Chanzon, Shenzhen, China) for 30 s. The LED is also programmed to move above the printed structure to make sure that all parts are fully cured. The distance between the LED and the printing substrate is fixed to 15 mm. Finally, the printed structures together with the glass substrates are post-treated by heating for 10 min using a 120 °C hot plate so that the M-SMP parts would be softened and easy to peel off from the substrate. The structures shown in Figure 3 are printed using one layer of filaments, and the distance between the nozzle tip and the glass substrate is 0.4 mm. The active metamaterial shown in Figures 4 and 5 are fabricated by directly stacking five layers of filaments, and the layer thickness is 0.4 mm.

Curable Depth Measurement. To measure the curable depth of M-SMP and MSM inks, two glass slides are used to sandwich the ink sample with 2 mm thick spacers. Then the samples are exposed to the 100-W UV LED with a distance of 15 mm for a period of time. After separating the two glass slides and wiping out the uncured ink, a layer of solidified ink is attached to the slide that directly faces the UV LED. The total thickness of the slide and cured ink t_{S+C} and the thickness of the slide t_S are measured. The curable depth is then calculated as $t_C = t_{S+C} - t_S$.

Mechanical and Magnetic Characterization of Materials. A dynamic mechanical analysis (DMA) instrument (DMA 850, TA Instruments, New Castle, DE, USA) is utilized to conduct the uniaxial tension tests and dynamic thermomechanical tests. The dimension of the printed specimens for both mechanical tests is 20 mm × 4 mm × 0.4 mm (one layer, the filament length is 20 mm). In the uniaxial tensile tests, the strain rate is set to 0.02 min⁻¹. In the dynamic thermomechanical tests, the specimens are oscillated at 1 Hz with 0.4% strain, sweeping from 22 to 105 °C using a rate of 3 °C min⁻¹. A vibrating sample magnetometer (VSM, 7400A series, Lake Shore Crytronics, Inc., Chicago, IL, USA) is utilized for the static remanence characterization. The dimension of the printed specimens for magnetic tests is 4 mm × 4 mm × 0.4 mm (one layer). The magnetic moment density is obtained by dividing the measured magnetic moment by the volume of the specimen. The Young's moduli of M-SMP at 90 °C and MSM at 22 and 90 °C are estimated on the basis of the secant moduli at 0.05 strain, whereas Young's modulus of M-SMP at 22 °C is based on the secant modulus at 0.002 strain because of the material's glassy behavior and the low strain during actuation.

Finite Element Simulation. A user-defined 8-node linear hexahedral element subroutine[44] is applied in the commercial FE software ABAQUS 2018 (Dassault System, Dassault System, Providence, RI, USA) to predict the responses of the magnetic-responsive materials following an incompressible hyperelastic constitutive model. The magnetic moment densities, external magnetic fields, and Young's moduli of the materials are used as input for the simulation. Different Young's moduli are used to simulate the material at 22 and 90 °C operating temperatures.

Actuation Experiments of Pop-up Structures and Active Metamaterials. For the actuation, a set of single-axis Helmholtz coils is utilized to generate a 1D magnetic field with controllable time and magnitude. For the heating, the pop-up structures are heated by an in-house built Joule-heating hot plate. While all the experiments of the active metamaterials are conveyed in a water tank to apply a uniform temperature field to the whole structure. To prevent the out-of-plane

deformation in the experiments, a supported acrylic plate is covered above the active metamaterials. The average wall thickness of the printed filament is measured as 0.67 mm and is used for the simulations.

ASSOCIATED CONTENT

SI **Supporting Information**

The Supporting Information is available free of charge at https://pubs.acs.org/doi/10.1021/acsami.0c13863.

> Figures including chemical structures of the components in the resins; enlarged Figure 2c; strain measurements of the active metamaterials (PDF)
>
> Video S1, multimodal pop-up structures MP4)
>
> Video S2, active metamaterial with tunable properties and shiftable mechanical behaviors—a chiral design (MP4)
>
> Video S3, active metamaterial with tunable properties and shiftable mechanical behaviors—an hourglass design (MP4)

AUTHOR INFORMATION

Corresponding Author

> **Ruike Zhao** − *Department of Mechanical and Aerospace Engineering, The Ohio State University, Columbus, Ohio 43210, United States;* ⊙ orcid.org/0000-0002-9292-5267; Email: zhao.2885@osu.edu

Authors

> **Chunping Ma** − *Department of Mechanical and Aerospace Engineering, The Ohio State University, Columbus, Ohio 43210, United States*
>
> **Shuai Wu** − *Department of Mechanical and Aerospace Engineering, The Ohio State University, Columbus, Ohio 43210, United States*
>
> **Qiji Ze** − *Department of Mechanical and Aerospace Engineering, The Ohio State University, Columbus, Ohio 43210, United States*
>
> **Xiao Kuang** − *The George W. Woodruff School of Mechanical Engineering, Georgia Institute of Technology, Atlanta, Georgia 30332, United States;* ⊙ orcid.org/0000-0001-6596-1417
>
> **Rundong Zhang** − *Department of Mechanical and Aerospace Engineering, The Ohio State University, Columbus, Ohio 43210, United States*
>
> **H. Jerry Qi** − *The George W. Woodruff School of Mechanical Engineering, Georgia Institute of Technology, Atlanta, Georgia 30332, United States;* ⊙ orcid.org/0000-0002-3212-5284

Complete contact information is available at:
https://pubs.acs.org/10.1021/acsami.0c13863

Author Contributions

[†]C.M. and S.W. contributed equally to this work.

Notes

The authors declare no competing financial interest.

REFERENCES

(1) Ge, Q.; Sakhaei, A. H.; Lee, H.; Dunn, C. K.; Fang, N. X.; Dunn, M. L. Multimaterial 4D Printing with Tailorable Shape Memory Polymers. *Sci. Rep.* **2016**, *6* (1), 31110.

(2) Boley, J. W.; van Rees, W. M.; Lissandrello, C.; Horenstein, M. N.; Truby, R. L.; Kotikian, A.; Lewis, J. A.; Mahadevan, L. Shape-Shifting Structured Lattices via Multimaterial 4D Printing. *Proc. Natl. Acad. Sci. U. S. A.* **2019**, *116* (42), 20856−20862.

(3) Ding, Z.; Yuan, C.; Peng, X.; Wang, T.; Qi, H. J.; Dunn, M. L. Direct 4D Printing via Active Composite Materials. *Sci. Adv.* **2017**, *3* (4), e1602890.

(4) Donovan, B. R.; Matavulj, V. M.; Ahn, S.; Guin, T.; White, T. J. All-Optical Control of Shape. *Adv. Mater.* **2019**, *31* (2), 1805750.

(5) Iamsaard, S.; Aßhoff, S. J.; Matt, B.; Kudernac, T.; Cornelissen, J. J. L. M.; Fletcher, S. P.; Katsonis, N. Conversion of Light into Macroscopic Helical Motion. *Nat. Chem.* **2014**, *6* (3), 229−235.

(6) Liu, Y.; Shaw, B.; Dickey, M. D.; Genzer, J. Sequential Self-Folding of Polymer Sheets. *Sci. Adv.* **2017**, *3* (3), e1602417.

(7) Christianson, C.; Goldberg, N. N.; Deheyn, D. D.; Cai, S.; Tolley, M. T. Translucent Soft Robots Driven by Frameless Fluid Electrode Dielectric Elastomer Actuators. *Sci. Robot.* **2018**, *3* (17), eaat1893.

(8) Acome, E.; Mitchell, S. K.; Morrissey, T. G.; Emmett, M. B.; Benjamin, C.; King, M.; Radakovitz, M.; Keplinger, C. Hydraulically Amplified Self-Healing Electrostatic Actuators with Muscle-like Performance. *Science* **2018**, *359* (6371), 61−65.

(9) Huang, H.-W.; Sakar, M. S.; Petruska, A. J.; Pané, S.; Nelson, B. J. Soft Micromachines with Programmable Motility and Morphology. *Nat. Commun.* **2016**, *7* (1), 12263.

(10) Lum, G. Z.; Ye, Z.; Dong, X.; Marvi, H.; Erin, O.; Hu, W.; Sitti, M. Shape-Programmable Magnetic Soft Matter. *Proc. Natl. Acad. Sci. U. S. A.* **2016**, *113* (41), E6007−E6015.

(11) Hu, W.; Lum, G. Z.; Mastrangeli, M.; Sitti, M. Small-Scale Soft-Bodied Robot with Multimodal Locomotion. *Nature* **2018**, *554* (7690), 81−85.

(12) Wehner, M.; Truby, R. L.; Fitzgerald, D. J.; Mosadegh, B.; Whitesides, G. M.; Lewis, J. A.; Wood, R. J. An Integrated Design and Fabrication Strategy for Entirely Soft, Autonomous Robots. *Nature* **2016**, *536* (7617), 451−455.

(13) Wu, S.; Hamel, C. M.; Ze, Q.; Yang, F.; Qi, H. J.; Zhao, R. Evolutionary Algorithm-Guided Voxel-Encoding Printing of Functional Hard-Magnetic Soft Active Materials. *Adv. Intell. Syst.* **2020**, 2000060.

(14) Schaffner, M.; Faber, J. A.; Pianegonda, L.; Rühs, P. A.; Coulter, F.; Studart, A. R. 3D Printing of Robotic Soft Actuators with Programmable Bioinspired Architectures. *Nat. Commun.* **2018**, *9* (1), 878.

(15) Sundaram, S.; Skouras, M.; Kim, D. S.; van den Heuvel, L.; Matusik, W. Topology Optimization and 3D Printing of Multimaterial Magnetic Actuators and Displays. *Sci. Adv.* **2019**, *5* (7), eaaw1160.

(16) Zhang, Y.-F.; Zhang, N.; Hingorani, H.; Ding, N.; Wang, D.; Yuan, C.; Zhang, B.; Gu, G.; Ge, Q. Fast-Response, Stiffness-Tunable Soft Actuator by Hybrid Multimaterial 3D Printing. *Adv. Funct. Mater.* **2019**, *29* (15), 1806698.

(17) Zhang, H.; Guo, X.; Wu, J.; Fang, D.; Zhang, Y. Soft Mechanical Metamaterials with Unusual Swelling Behavior and Tunable Stress-Strain Curves. *Sci. Adv.* **2018**, *4* (6), eaar8535.

(18) Wu, S.; Ze, Q.; Zhang, R.; Hu, N.; Cheng, Y.; Yang, F.; Zhao, R. Symmetry-Breaking Actuation Mechanism for Soft Robotics and Active Metamaterials. *ACS Appl. Mater. Interfaces* **2019**, *11* (44), 41649−41658.

(19) Kim, Y.; Parada, G. A.; Liu, S.; Zhao, X. Ferromagnetic Soft Continuum Robots. *Sci. Robot.* **2019**, *4* (33), eaax7329.

(20) Jeon, S.; Hoshiar, A. K.; Kim, K.; Lee, S.; Kim, E.; Lee, S.; Kim, J.; Nelson, B. J.; Cha, H.-J.; Yi, B.-J.; Choi, H. A Magnetically Controlled Soft Microrobot Steering a Guidewire in a Three-Dimensional Phantom Vascular Network. *Soft Robot.* **2019**, *6* (1), 54−68.

(21) Lind, J. U.; Busbee, T. A.; Valentine, A. D.; Pasqualini, F. S.; Yuan, H.; Yadid, M.; Park, S.; Kotikian, A.; Nesmith, A. P.; Campbell, P. H.; Vlassak, J. J.; Lewis, J. A.; Parker, K. K. Instrumented Cardiac Microphysiological Devices via Multimaterial Three-Dimensional Printing. *Nat. Mater.* **2017**, *16* (3), 303−308.

(22) Kim, J.; Chung, S. E.; Choi, S.-E.; Lee, H.; Kim, J.; Kwon, S. Programming Magnetic Anisotropy in Polymeric Microactuators. *Nat. Mater.* **2011**, *10* (10), 747−752.

(23) Ren, Z.; Hu, W.; Dong, X.; Sitti, M. Multi-Functional Soft-Bodied Jellyfish-like Swimming. *Nat. Commun.* **2019**, *10* (1), 2703.

(24) Kuang, X.; Roach, D.; Hamel, C.; Yu, K.; Qi, J. Materials, Design and Fabrication of Shape Programmable Polymers. *Multifunct. Mater.* **2020**, DOI: 10.1088/2399-7532/aba1d9.

(25) Kim, Y.; Yuk, H.; Zhao, R.; Chester, S. A.; Zhao, X. Printing Ferromagnetic Domains for Untethered Fast-Transforming Soft Materials. *Nature* **2018**, *558* (7709), 274−279.

(26) Ze, Q.; Kuang, X.; Wu, S.; Wong, J.; Montgomery, S. M.; Zhang, R.; Kovitz, J. M.; Yang, F.; Qi, H. J.; Zhao, R. Magnetic Shape Memory Polymers with Integrated Multifunctional Shape Manipulation. *Adv. Mater.* **2020**, *32* (4), 1906657.

(27) Kuang, X.; Wu, J.; Chen, K.; Zhao, Z.; Ding, Z.; Hu, F.; Fang, D.; Qi, H. J. Grayscale Digital Light Processing 3D Printing for Highly Functionally Graded Materials. *Sci. Adv.* **2019**, *5* (5), eaav5790.

(28) Kokkinis, D.; Bouville, F.; Studart, A. R. 3D Printing of Materials with Tunable Failure via Bioinspired Mechanical Gradients. *Adv. Mater.* **2018**, *30* (19), 1705808.

(29) Wu, L.; Li, B.; Zhou, J. Isotropic Negative Thermal Expansion Metamaterials. *ACS Appl. Mater. Interfaces* **2016**, *8* (27), 17721−17727.

(30) Takezawa, A.; Kobashi, M. Design Methodology for Porous Composites with Tunable Thermal Expansion Produced by Multi-Material Topology Optimization and Additive Manufacturing. *Composites, Part B* **2017**, *131*, 21−29.

(31) Li, Y.; Chen, Y.; Li, T.; Cao, S.; Wang, L. Hoberman-Sphere-Inspired Lattice Metamaterials with Tunable Negative Thermal Expansion. *Compos. Struct.* **2018**, *189*, 586−597.

(32) Liu, J.; Gu, T.; Shan, S.; Kang, S. H.; Weaver, J. C.; Bertoldi, K. Harnessing Buckling to Design Architected Materials That Exhibit Effective Negative Swelling. *Adv. Mater.* **2016**, *28* (31), 6619−6624.

(33) Chen, D.; Zheng, X. Multi-Material Additive Manufacturing of Metamaterials with Giant, Tailorable Negative Poisson's Ratios. *Sci. Rep.* **2018**, *8* (1), 9139.

(34) Miri, A. K.; Nieto, D.; Iglesias, L.; Goodarzi Hosseinabadi, H.; Maharjan, S.; Ruiz-Esparza, G. U.; Khoshakhlagh, P.; Manbachi, A.; Dokmeci, M. R.; Chen, S.; Shin, S. R.; Zhang, Y. S.; Khademhosseini, A. Microfluidics-Enabled Multimaterial Maskless Stereolithographic Bioprinting. *Adv. Mater.* **2018**, *30* (27), 1800242.

(35) Han, D.; Yang, C.; Fang, N. X.; Lee, H. Rapid Multi-Material 3D Printing with Projection Micro-Stereolithography Using Dynamic Fluidic Control. *Addit. Manuf.* **2019**, *27*, 606−615.

(36) Mansouri, M. R.; Montazerian, H.; Schmauder, S.; Kadkhodapour, J. 3D-Printed Multimaterial Composites Tailored for Compliancy and Strain Recovery. *Compos. Struct.* **2018**, *184*, 11−17.

(37) Loke, G.; Yuan, R.; Rein, M.; Khudiyev, T.; Jain, Y.; Joannopoulos, J.; Fink, Y. Structured Multimaterial Filaments for 3D Printing of Optoelectronics. *Nat. Commun.* **2019**, *10* (1), 4010.

(38) Matsuzaki, R.; Kanatani, T.; Todoroki, A. Multi-Material Additive Manufacturing of Polymers and Metals Using Fused Filament Fabrication and Electroforming. *Addit. Manuf.* **2019**, *29*, 100812.

(39) Schwartz, J. J.; Boydston, A. J. Multimaterial Actinic Spatial Control 3D and 4D Printing. *Nat. Commun.* **2019**, *10* (1), 791.

(40) Skylar-Scott, M. A.; Mueller, J.; Visser, C. W.; Lewis, J. A. Voxelated Soft Matter via Multimaterial Multinozzle 3D Printing. *Nature* **2019**, *575* (7782), 330−335.

(41) Kokkinis, D.; Schaffner, M.; Studart, A. R. Multimaterial Magnetically Assisted 3D Printing of Composite Materials. *Nat. Commun.* **2015**, *6* (1), 8643.

(42) Chen, K.; Zhang, L.; Kuang, X.; Li, V.; Lei, M.; Kang, G.; Wang, Z. L.; Qi, H. J. Dynamic Photomask-Assisted Direct Ink Writing Multimaterial for Multilevel Triboelectric Nanogenerator. *Adv. Funct. Mater.* **2019**, *29* (33), 1903568.

(43) Roach, D. J.; Hamel, C. M.; Dunn, C. K.; Johnson, M. V.; Kuang, X.; Qi, H. J. The M4 3D Printer: A Multi-Material Multi-Method Additive Manufacturing Platform for Future 3D Printed Structures. *Addit. Manuf.* **2019**, *29*, 100819.

(44) Zhao, R.; Kim, Y.; Chester, S. A.; Sharma, P.; Zhao, X. Mechanics of Hard-Magnetic Soft Materials. *J. Mech. Phys. Solids* **2019**, *124*, 244−263.

(45) Montgomery, S. M.; Wu, S.; Kuang, X.; Armstrong, C. D.; Zemelka, C.; Ze, Q.; Zhang, R.; Zhao, R.; Qi, H. J. Magneto-Mechanical Metamaterials with Widely Tunable Mechanical Properties and Acoustic Bandgaps. *arXiv (Physics.Applied Physics)*, June 23,2020, 2006.12721v1. https://arxiv.org/ftp/arxiv/papers/2006/2006.12721.pdf.

(46) Bodaghi, M.; Damanpack, A. R.; Liao, W. H. Adaptive Metamaterials by Functionally Graded 4D Printing. *Mater. Des.* **2017**, *135*, 26−36.

(47) Jackson, J. A.; Messner, M. C.; Dudukovic, N. A.; Smith, W. L.; Bekker, L.; Moran, B.; Golobic, A. M.; Pascall, A. J.; Duoss, E. B.; Loh, K. J.; Spadaccini, C. M. Field Responsive Mechanical Metamaterials. *Sci. Adv.* **2018**, *4* (12), eaau6419.

(48) Overvelde, J. T. B.; Shan, S.; Bertoldi, K. Compaction Through Buckling in 2D Periodic, Soft and Porous Structures: Effect of Pore Shape. *Adv. Mater.* **2012**, *24* (17), 2337−2342.

(49) Clausen, A.; Wang, F.; Jensen, J. S.; Sigmund, O.; Lewis, J. A. Topology Optimized Architectures with Programmable Poisson's Ratio over Large Deformations. *Adv. Mater.* **2015**, *27* (37), 5523−5527.

(50) Coulais, C.; Teomy, E.; de Reus, K.; Shokef, Y.; van Hecke, M. Combinatorial Design of Textured Mechanical Metamaterials. *Nature* **2016**, *535* (7613), 529−532.

(51) Tang, Y.; Lin, G.; Yang, S.; Yi, Y. K.; Kamien, R. D.; Yin, J. Programmable Kiri-Kirigami Metamaterials. *Adv. Mater.* **2017**, *29* (10), 1604262.

(52) Coulais, C. As the Extension, so the Twist. *Science* **2017**, *358* (6366), 994−995.

(53) Shan, S.; Kang, S. H.; Zhao, Z.; Fang, L.; Bertoldi, K. Design of Planar Isotropic Negative Poisson's Ratio Structures. *Extreme Mech. Lett.* **2015**, *4*, 96−102.